High Power Laser Science and Engineering, (2021), Vol. 9, e9, 8 pages.
doi:10.1017/hpl.2020.49

HIGH POWER LASER SCIENCE AND ENGINEERING

RESEARCH ARTICLE

Emission mechanism for the silicon He-α lines in a photoionization experiment

Bo Han[1,2], Feilu Wang[3,4,5], David Salzmann[3], Jiayong Zhong[1,6], and Gang Zhao[3,4]

[1] *Department of Astronomy, Beijing Normal University, Beijing 100875, China*

[2] *College of Physics and Electronic Engineering, Qilu Normal University, Jinan 250200, China*

[3] *CAS Key Laboratory of Optical Astronomy, National Astronomical Observatories, Chinese Academy of Sciences, Beijing 100101, China*

[4] *School of Astronomy and Space Science, University of Chinese Academy of Sciences, Beijing 101408, China*

[5] *Graduate School of China Academy of Engineering Physics, Beijing 100196, China*

[6] *Collaborative Innovation Center of IFSA (CICIFSA), Shanghai Jiao Tong University, Shanghai 200240, China*

(Received 22 June 2020; revised 24 October 2020; accepted 26 November 2020)

Abstract

In this paper, we present a reanalysis of the silicon He-α X-ray spectrum emission in Fujioka *et al.*'s 2009 photoionization experiment. The computations were performed with our radiative-collisional code, RCF. The central ingredients of our computations are accurate atomic data, inclusion of satellite lines from doubly excited states and accounting for the reabsorption of the emitted photons on their way to the spectrometer. With all these elements included, the simulated spectrum turns out to be in good agreement with the experimental spectrum.

Keywords: high-energy-density physics; laboratory astrophysics; laser–plasma interaction

1. Introduction

The concept of photoionizing plasmas[1–5] was first introduced by Tarter, Tucker and Salpeter (1969)[6] to explain X-ray spectra from highly ionized but low-temperature celestial objects. Since then, more astronomical sources with similar spectral properties have been observed[7–9]. These are either diffuse sources (interstellar gas, supernova remnants, etc.) or high-mass X-ray binary systems (HMXBs) around compact objects (black holes, neutron stars, white dwarfs)[7–11].

In recent years there have also been a few attempts to produce photoionizing plasmas in the laboratory under controlled experimental conditions[12,13]. Several problems make such experiments extremely difficult. The first one is, of course, the generation of a high-intensity X-ray beam that can ionize high-Z material to He- and H-like species. This requires extreme technology such as the Z machine[12] or high-intensity lasers[13,14]. A second difficulty is the analysis of such experiments: while astrophysical photoionizing plasmas are stable, time-independent objects, laboratory plasmas vary on timescales of nanoseconds and spatial extents of micrometers. Nevertheless, both kinds of plasmas produce He-α triplet lines: the central diagnostic tool in the analysis of photoionizing plasmas[15].

The main aim of this paper is a new analysis of the experiment of Fujioka *et al.*, which was carried out on the GEKKO-XII laser facility. In this experiment a blackbody (BB) radiation source with temperature of $T_r = 480 \pm 20$ eV was generated by converging 12 high-intensity laser beams on a CH_2 pellet, with the experimental dilution factor $a = (6.5 \pm 3.5) \times 10^{-4}$. The Planck radiation from this source was used to irradiate, through a narrow slit, a low-temperature silicon plasma having electron density $n_e = (0.75 \pm 0.25) \times 10^{20}$ cm^{-3} [13], which was generated simultaneously. The central measurement of the experiment is the He-α triplet spectrum from the silicon plasma in the range of 1820–1865 eV, as well as the electron temperature, which was measured to be $T_e = 27.5 \pm 1.5$ eV. A photoionized silicon plasma was produced, whose ionization parameter, $\xi = 16\pi^2 J/n_e$, reached (5.9±3.8) erg·cm·s^{-1} (J is the radiation intensity and n_e is the electron density).

Correspondence to: F. Wang, CAS Key Laboratory of Optical Astronomy, National Astronomical Observatories, Chinese Academy of Sciences, Beijing 100101, China. Email: wfl@bao.ac.cn

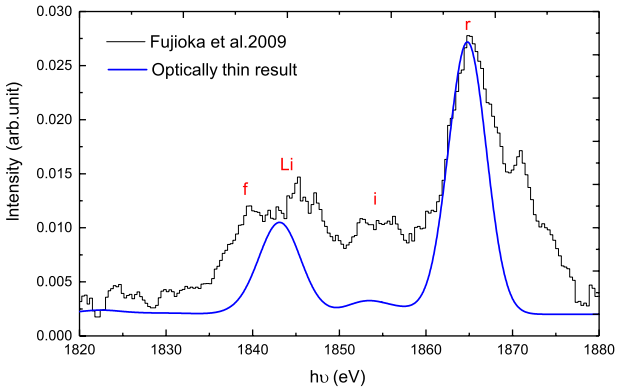

Figure 1. Black line: the experimental spectrum of Fujioka *et al.*[13]. Blue line: the theoretical result of an optically thin model. f, Li, i and r denote the position of the forbidden line, satellite lines, the intercombination line and the resonance line, respectively.

The experimental spectrum is shown in Figure 1, and it contains the three He-α triplet peaks. The peak at 1864 eV is the resonance line ($1s^2\ ^1S_0$-$1s2p\ ^1P_2$) and the peak at 1855 eV is the intercombination line ($1s^2\ ^1S_0$-$1s2p\ ^3P_2$ and $1s^2\ ^1S_0$-$1s2p\ ^3P_1$), whose reproduction was the aim of the aforementioned papers and this paper as well[13,16–20]. The forbidden line ($1s^2\ ^1S_0$-$1s2s\ ^3S_1$) is expected to show up around 1840 eV and is supposed to be negligibly low. Wang *et al*. employed a relatively simple time-dependent model, which included only photoionization and radiative recombination as the main atomic processes. Using this model they could reproduce correctly the average plasma properties, such as the plasma temperature and the average ionization degree, $\overline{Z}$, and their behavior as a function of time. Their simulated spectrum, however, could not reproduce correctly the experimental He-α spectrum and in particular the ratio between the intercombination and the resonance peaks.

Several studies tried to overcome the mismatch between the simulated and measured spectra. Hill and Rose used a detailed configuration for recording atomic data in a time-dependent model. They also added opacity effects into the simulation. They correctly predicted the resonance line, but the time-dependent relative intensities were always different from those in the experimental results. Later, Bao *et al*. simulated the spectrum with a steady-state model. While their simulated peaks around 1864 eV and 1840 eV fitted the experimental peaks, the peak at 1855 eV was weaker than the experimental value. Wu *et al*. developed a time-dependent model, but, similarly, their central peak was still too low. As a matter of fact, all these papers report results that are not significantly different from those of Wang *et al*. in Figure 1.

In this study we reanalyzed the results obtained by Fujioka *et al.*[13,14]. Based on assumed very high accuracy atomic data, this work focuses on the detailed contributions of every atomic process to investigate the line emission mechanism under experimental conditions. Our analysis also takes the opacity effect into account. The line emission mechanism is investigated with three models: (i) a steady-state optically thin model; (ii) a time-dependent optically thin model; and finally (iii) a steady-state optically thick model. With all these elements in our simulations, we finally succeeded to obtain reasonably good agreement between our third model and the experiment.

A brief description of the theoretical model and comparisons of atomic data are given in Section 2. In Section 3, the line emission mechanism is investigated under experimental conditions, and the reason for the weak central peak in previous studies is explained. Finally, a summary is given in Section 4.

2. Theoretical model

In the computations presented in this paper, we use radiative-collisional code based on FAC (RCF)[21,22] to calculate the spectrum emitted from a photoionizing plasma. RCF is collisional-radiative code that simulates plasma under nonlocal thermodynamic equilibrium conditions. RCF takes into account ten atomic processes in the rate equations to calculate the charge state distribution, the level distribution and the corresponding spectrum. The atomic processes are divided into five mutually inverse groups[21,23]. Two of these groups are (i) free electron collisional ionization (CI) and three-body recombination (TR); and (ii) electron collisional excitation (CE) and collisional deexcitation (CD). The other three groups include the photon-induced processes that take place when a plasma is irradiated by a strong radiation field, which may turn out to become the dominant processes: (iii) photoionization (PI) and radiative recombination (RR); (iv) photoexcitation (PE) of ionic levels and subsequent spontaneous radiative decay (A); and (v) autoionization (AI) and dielectronic capture (DC) – doubly excited states can ionize spontaneously by AI or be produced through DC, which eventually decay to ground state through emission of the corresponding satellite lines.

The relevant atomic data, such as the energy levels, cross-sections and rate coefficients of these processes, are calculated by flexible atomic code (FAC)[24]. FAC solves the relativistic Dirac equation for the given atom/ion in a j–j coupling scheme. Charge states from bare nuclei down to C-like and levels up to $n = 8$ are included in the present calculations[25]. The accuracy of atomic data has been checked for several conditions in our previous publications[21,25]. Comparisons of the atomic data in this study with the data in others are shown in Table 1 and Figure 2. In Table 1, the energies and Einstein A coefficients of the 29 strongest lines are listed. They show good agreement within 0.05% and 10%, respectively, when compared with the data from Palmeri *et al*. Comparisons of the collisional excitation cross-sections for transitions among the 1s2l levels of silicon with data from the NIFS database[26–29] are shown in Figure 2, which also show good agreement. The

https://doi.org/10.1017/hpl.2020.49 Published online by Cambridge University Press

Table 1. Transition energies and Einstein A coefficients of some intense silicon lines between 1820 eV and 1865 eV. The resonance, intercombination and forbidden lines are marked as R/w, $I/(x+y)$ and F/z, respectively.

Ion	Transition				This study		Palmeri *et al.*	
	Upper		Lower		Energy (eV)	A (s^{-1})	Energy (eV)	A (s^{-1})
He-like	1s2p	$^1P_1$	$1s^2$	$^1S_0$	1864.8115 (R/w)	3.87×10^{13}	1864.979804	4.07×10^{13}
Li-like	1s2p(1P)3d	$^2F_{5/2}$	$1s^23d$	$^2D_{3/2}$	1863.774295	2.50×10^{13}		
Li-like	1s2p(1P)3d	$^2F_{7/2}$	$1s^23d$	$^2D_{5/2}$	1863.326131	2.90×10^{13}		
Li-like	1s2p(1P)3d	$^2D_{5/2}$	$1s^23d$	$^2D_{5/2}$	1861.843125	3.14×10^{13}		
Li-like	1s2p(1P)3d	$^2D_{3/2}$	$1s^23d$	$^2D_{3/2}$	1861.815167	3.29×10^{13}		
Li-like	1s2p(1P)3s	$^2P_{1/2}$	$1s^23s$	$^2S_{1/2}$	1861.284114	2.73×10^{13}		
Li-like	1s2p(1P)3s	$^2P_{3/2}$	$1s^23s$	$^2S_{1/2}$	1861.116476	1.54×10^{13}		
Li-like	1s2p(1P)3p	$^2P_{3/2}$	$1s^23p$	$^2P_{3/2}$	1860.781291	3.24×10^{13}		
Li-like	1s2p(1P)3p	$^2D_{3/2}$	$1s^23p$	$^2P_{1/2}$	1860.641666	2.88×10^{13}		
Li-like	1s2p(1P)3p	$^2P_{1/2}$	$1s^23p$	$^2P_{1/2}$	1860.641666	2.59×10^{13}		
Li-like	1s2p(1P)3p	$^2D_{5/2}$	$1s^23p$	$^2P_{3/2}$	1860.334565	2.88×10^{13}		
Li-like	$1s(2S)2p^2$	$^2S_{1/2}$	$1s^23p$	$^2P_{3/2}$	1856.073555	1.21×10^{13}	1856.712852	1.27×10^{13}
Li-like	1s(2S)2s2p(1P)	$^2P_{3/2}$	$1s^22s$	$^2S_{1/2}$	1854.047395	7.36×10^{12}	1854.546585	2.82×10^{12}
Li-like	1s(2S)2s2p(1P)	$^2P_{1/2}$	$1s^22s$	$^2S_{1/2}$	1853.881058	4.89×10^{12}	1854.213762	4.96×10^{12}
He-like	1s2p	$^3P_1$	$1s^2$	$^1S_0$	1853.8562 (I/x)	3.77×10^{7}		
He-like	1s2p	$^3P_2$	$1s^2$	$^1S_0$	1852.9801 (I/y)	1.36×10^{11}		
Li-like	1s(2S)2s2p(3P)	$^2P_{3/2}$	$1s^22s$	$^2S_{1/2}$	1844.805711	3.26×10^{13}	1845.657041	3.50×10^{13}
Li-like	1s(2S)2s2p(3P)	$^2P_{1/2}$	$1s^22s$	$^2S_{1/2}$	1844.229449	3.06×10^{13}	1845.107706	3.29×10^{13}
Li-like	$1s(2S)2p^2(3P)$	$^2P_{1/2}$	$1s^22p$	$^2P_{3/2}$	1842.858845	4.67×10^{13}	1842.448061	1.76×10^{13}
Li-like	$1s(2S)2p^2(1D)$	$^2D_{5/2}$	$1s^22p$	$^2P_{1/2}$	1840.232989	1.81×10^{13}	1840.478845	1.85×10^{13}
Li-like	$1s(2S)2p^2(1D)$	$^2D_{3/2}$	$1s^22p$	$^2P_{3/2}$	1839.113808	1.75×10^{13}	1839.577694	1.82×10^{13}
He-like	1s2s	$^3S_1$	$1s^2$	$^1S_0$	1838.2023 (F/z)	3.27×10^{5}		
Be-like	$1s2p^3$	$^1P_1$	$1s^22p^2$	$^1D_2$	1831.236355	2.61×10^{13}	1831.128172	2.81×10^{13}
Be-like	$1s2s^22p$	$^1P_1$	$1s^22s^2$	$^1S_0$	1828.346862	3.21×10^{13}	1828.185104	3.48×10^{13}
Be-like	$1s(2S)2s2p^2(2S)$	$^1S_0$	$1s^22s2p$	$^1P_1$	1827.107451	1.79×10^{13}	1827.996423	1.64×10^{13}
Be-like	$1s(2S)2s2p^2(2P)$	$^1P_1$	$1s^22s2p$	$^1P_1$	1827.107451	4.91×10^{13}	1827.484485	5.32×10^{13}
Be-like	$1s(2S)2s2p^2(4P)$	$^3P_2$	$1s^22p^2$	$^3P_2$	1823.640658	4.65×10^{13}	1823.426096	4.25×10^{13}
Be-like	$1s(2S)2s2p^2(2D)$	$^3D_2$	$1s^22ssp$	$^3P_1$	1823.587013	2.40×10^{13}	1823.077541	2.18×10^{13}
Be-like	$1s(2S)2s2p^2(2D)$	$^3D_1$	$1s^22ssp$	$^3P_0$	1823.533371	2.28×10^{13}	1823.318834	2.53×10^{13}

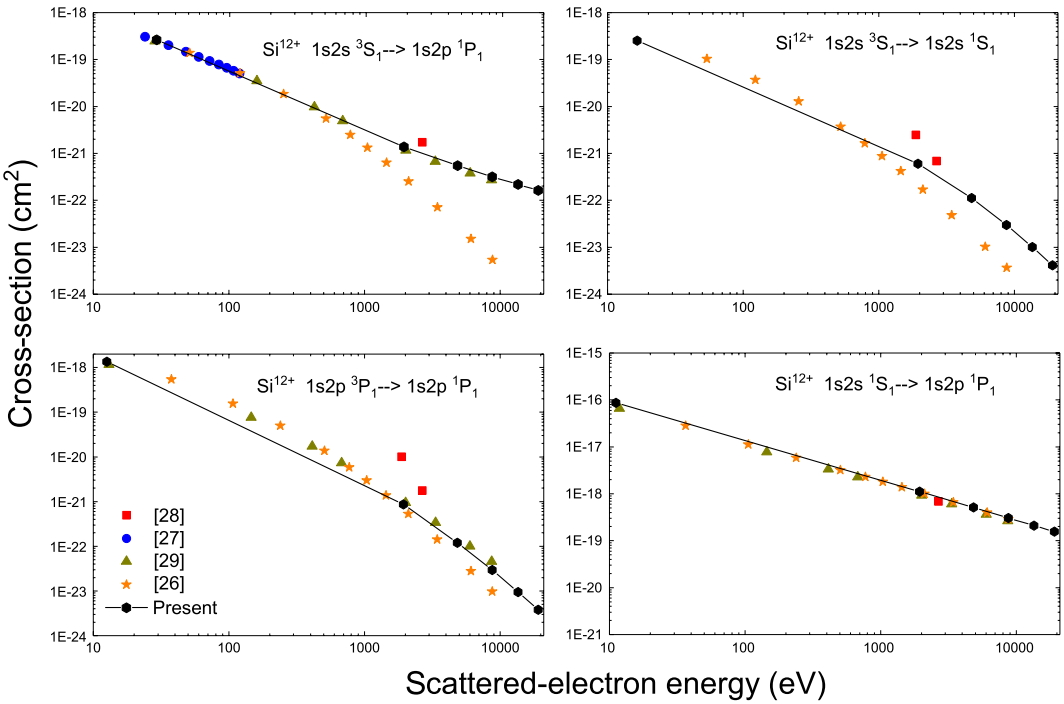

Figure 2. Comparison of the collisional excitation cross-section with the results of Refs. [26–29]. The transitions include $1s2s\ ^3S_1 \rightarrow 1s2p\ ^1P_1$, $1s2s\ ^3S_1 \rightarrow 1s2s\ ^1S_1$, $1s2p\ ^3P_1 \rightarrow 1s2p\ ^1P_1$ and $1s2s\ ^1S_1 \rightarrow 1s2p\ ^1P_1$ of He-like Si.

https://doi.org/10.1017/hpl.2020.49 Published online by Cambridge University Press

Stewart–Pyatt continuum lowering formula[30] is taken into account for the high-density conditions, above $n_e \sim 10^{20}$ cm^{-3}. More details about the calculation of the various atomic processes are given in Ref. [21]. The simulated emission lines were broadened with a Gaussian profile having FWHM of 7 eV.

3. Results and discussion

Three models were used in our study.

Model 1: The plasma is assumed to be in a steady state, having constant density and temperature throughout the period of the irradiation. It is assumed also to be optically thin.

Model 2: The time dependence of the charge state distribution in the plasma is taken into account, but the model still assumes an optically thin plasma.

Model 3: A steady-state but optically thick plasma is assumed that accounts for the reabsorption of the emerging radiation inside the irradiated plasma.

The line emission mechanism is investigated with all three models, and the differences between the results, in particular the opacity effects, are explained and discussed.

3.1. Model 1: steady-state optically thin model

For the steady-state model, the rate equations used to calculate the charge state distribution are written in a shortened form,

$$\frac{\mathrm{d}N_{i,j}}{\mathrm{d}t} = \sum_{p}\sum_{m=i,i\pm1}\sum_{n} N_{m,n}R^{p}_{m,n\to i,j} - N_{i,j}\sum_{d}\sum_{m=i,i\pm1}\sum_{n} R^{d}_{i,j\to m,n} = 0, \tag{1}$$

where $N_{i,j}$ and $N_{m,n}$ (cm^{-3}) are the densities of the jth level of charge states i and the nth level of charge states m, respectively, and $R^{p}_{m,n\to i,j}$ and $R^{d}_{i,j\to m,n}$ are the rate coefficients (cm$^3\cdot$s^{-1}) of populating and depopulating processes. The first term of Equation (1) denotes the rates of the aforementioned processes that populate $N_{i,j}$ while the second term denotes the rates of the processes that depopulate this level. The rate equations are solved with the restrictions $n_i = \sum N_{i,j}$ and $n_e = \sum iN_{i,j}$.

In this model the irradiated plasma and the BB source have the same values as in the experiment of Fujioka *et al.* The input parameters are radiation temperature $T_r = 500$ eV, dilution factor $a = 10^{-3}$, electron density $n_e = 5\times10^{19}$ cm^{-3} and electron temperature $T_e = 26$ eV, which are all in the experimental range. Under such conditions, photoionization dominates over electron impact ionization. Moreover, autoionization following photoexcitation also plays an important role[21]. The computed values of the ion fractions of Li-like, He-like and H-like ions are 38%, 54% and 2%, respectively. The simulated spectrum is shown in Figure 1. In a similar manner to the results of previous studies, the peaks at 1840 eV and 1864 eV are in agreement with the experimental ones, but the one at 1855 eV is still too weak.

In order to discover the reason for the disagreement between the experimental spectrum and the simulated one, we plotted the relative importance of the contributions of the various atomic processes to the population of four excited states that appear to be important in the spectral region of interest, as shown in Figure 3. These are the three He-like 1s2p ^{1,3}P$_1$ or 1p2s ^{1}S$_0$ levels and the doubly excited 1s2s2p ^{2}P$_{1/2}$ Li-like level, whose transitions to ground state generate the emission of the strongest spectral lines. Figure 3 shows the populating and depopulating contributions of every process for these levels. The populating contribution of process p from level i to level j is calculated by

$$\mathcal{P}_p = \frac{\sum_{m=i,i\pm1}\sum_{n} N_{m,n}R^{p}_{m,n\to i,j}}{\sum_{q}\sum_{m=i,i\pm1}\sum_{n} N_{m,n}R^{q}_{m,n\to i,j}}, \tag{2}$$

and the depopulating contribution of process d to $N_{i,j}$ is calculated by

$$\mathcal{D}_d = \frac{\sum_{m=i,i\pm1}\sum_{n} R^{d}_{i,j\to m,n}}{\sum_{q}\sum_{m=i,i\pm1}\sum_{n} R^{q}_{i,j\to m,n}}. \tag{3}$$

In Figure 3, the 1s2s2p ^{2}P$_{1/2}$ and 1s2p ^{1}P$_1$ states, which account for the two strongest lines in the simulation, have similar behavior. These two levels are first populated by photoexcitation and then depopulated by radiative decay. As shown in Table 1, the A coefficients of the transitions of these two levels to ground state are larger than 3.0×10^{13} s^{-1}, so the levels are rapidly depopulated by decay to ground state. In addition to these, there are several other Li-like and Be-like levels that have A coefficients around 3.0×10^{13} s^{-1}. These, also, are excited through photoexcitation and emit strong lines that contribute to the peak around 1845 eV.

At the electron temperature of $T_e = 26$ eV the collisional excitation from ground state to the 1s2l He-like levels (whose energies are about 1840–1860 eV above ground state) is negligibly small. Nevertheless, collisional processes dominate the redistribution of population among these excited levels, because the electrons' energy is close to the energy intervals between the 1s2l levels. As 1s2s ^{1}S$_0$ and 1s2p ^{3}P$_0$ are metastable states, the redistribution generates an accumulation of He-like ions in these metastable states and, as

https://doi.org/10.1017/hpl.2020.49 Published online by Cambridge University Press

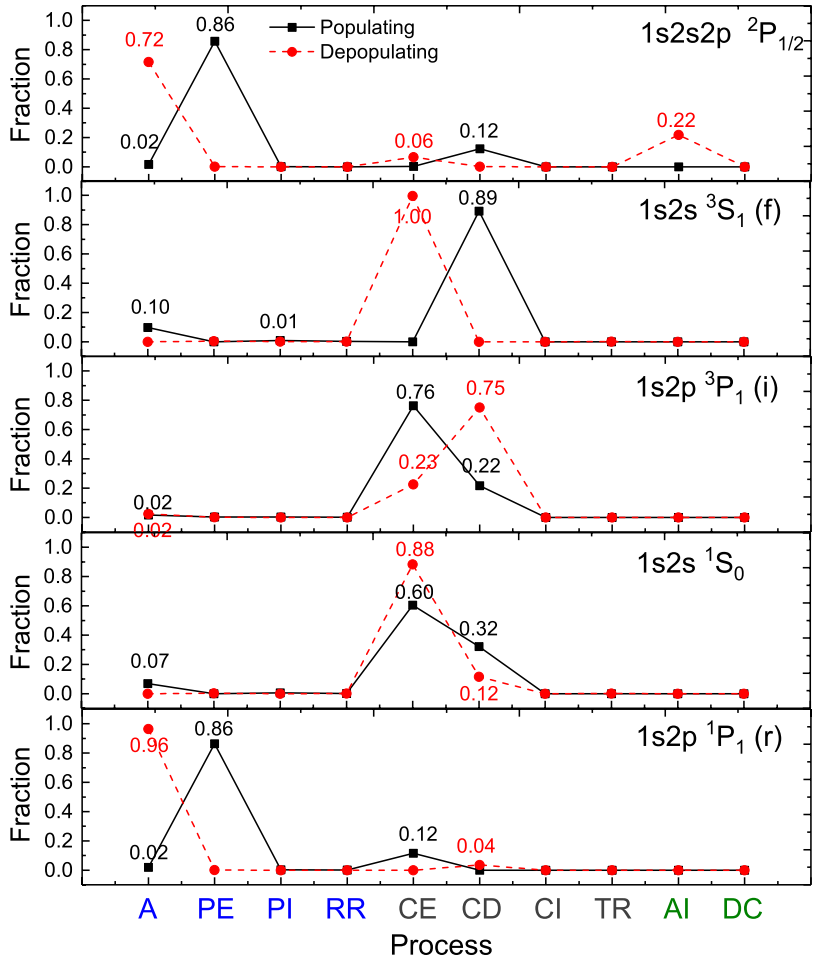

Figure 3. Contributions of atomic processes under the conditions of the Fujioka *et al*. photoionization experiment for five selected levels. The atomic processes are listed on the *x*-axis. The blue processes are related to the radiation field, the dark-gray processes are controlled by collisions and the green processes are autoionization and dielectronic capture. Solid black lines represent the populating contributions for the levels, and the red dashed lines represent the depopulating contributions for the levels. The contribution friction of each process is also labeled.

a consequence, they become overpopulated relative to the other 1s2l levels. Collisional processes then move the population from these metastable states to the allowed ones. Our computations indicate that about 12% of the 1s2p $^1P_1$ population is excited from the 1s2s $^1S_0$ and 1s2s $^3S_1$ metastable states by such collisions.

Altogether, this simulation shows that the main excitation of the He-like 1s2l levels is carried out through photoexcitation, but the collisional processes also have an important contribution through the redistribution of the excited states.

3.2. *Model 2: time-dependent optically thin model*

Next we tried to investigate the influence of a time-varying radiation pulse on the emission spectrum. For this purpose BB radiation having a Gaussian temporal profile was used,

$$G(t) = \exp\left[-\frac{(t-t_0)^2}{2\sigma^2}\right], \tag{4}$$

where $t_0 = 160$ ps and $\sigma \sim 80$ ps[13,16,20]. The rate equations in Model 2 take the form

$$\begin{aligned} N_{i,j}(t+\Delta t) &= N_{i,j}(t) + \Delta N_{i,j}(t) \\ &= N_{i,j}(t) + \Delta t \cdot \Big[\sum_p \sum_{m=i,i\pm1} \sum_n N_{m,n}(t) R^p_{m,n\to i,j}(t) \\ &\quad - N_{i,j}(t) \sum_d \sum_{m=i,i\pm1} \sum_n R^d_{i,j\to m,n}(t)\Big], \end{aligned} \tag{5}$$

where $N_{i,j}(t+\Delta t)$ is the level density at $t+\Delta t$, $N_{i,j}(t)$ and $N_{m,n}(t)$ are the level densities at the previous timestep, and $R^p_{m,n\to i,j}(t)$ and $R^d_{i,j\to m,n}(t)$ are the reaction rates at t. The electron temperature and density are assumed to be constant throughout the simulation[16,18,20]. To compensate for the lower incident energy in this model compared to Model 1, the dilution factor was increased to $a = 1\times10^{-2}$.

Figure 4 shows the temporal evolution of charge states up to 1 ns. The average charge state, $\overline{Z}$, reaches its maximum at the end of the radiation pulse and decreases slowly as

https://doi.org/10.1017/hpl.2020.49 Published online by Cambridge University Press

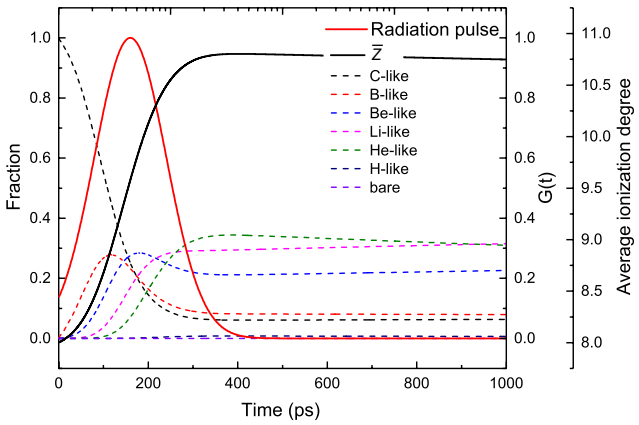

Figure 4. Evolution of fractions of charge states from C-like ion to bare nuclei in the time-dependent model with a Gaussian radiation pulse (red line). The radiation pulse is adapted as a Gaussian distribution with FWHM of 160 ps and $\sigma = 80$ ps[13,16,20].

the plasma cools. Figure 5 shows the contributions of the various atomic processes to the evolution of the 1s2p ^{1}P$_1$ level. This reflects also the behavior of the resonance line as a function of time. Figure 5 indicates that as the radiation pulse decreases, the level population is dominated by the collisional processes (CE and CD). In a similar manner to Model 1, the Li-like satellite lines might have similar behaviors. In Figure 6, the green line is the time-integrated spectrum. The resonance line and Li-like satellite lines are close to the experimental spectrum, but the peak around 1855 eV is still weak. In conclusion, the time-dependent optically thin model cannot reproduce the experimental spectrum.

3.3. *Model 3: steady-state optically thick model*

Finally, the opacity effects were added into Model 3. Recently, in the experiment of Loisel *et al*. on photoionized silicon plasma, optical depth up to 60 was measured for the He-like resonance line. This indicates that reabsorption along the line between the point of emission and the measuring device in the photoionization experiment has to be taken into account. As the assumption of time dependence of the incident pulse could not account for the difference between the experimental and simulated spectra, in Model 3 a steady-state plasma was used, as in Model 1.

To account for the opacity effect, i.e., photon reabsorption (PR) on the way to the spectrometer, we used the escape probability[31] method, i.e.,

$$I_{\rm abs}(\lambda) = I_0(\lambda)\, T(\lambda), \tag{6}$$

where λ is the photon wavelength, $I_{\rm abs}(\lambda)$ and $I_0(\lambda)$ are the absorbed and unabsorbed line intensities, respectively and $T(\lambda)$ is the transmittance of the absorbing medium,

$$T(\lambda) = \frac{1 - e^{-\tau(\lambda)}}{\tau(\lambda)}. \tag{7}$$

$\tau(\lambda)$ is the optical depth[32],

$$\tau(\lambda) = \tau_0 \phi(\lambda), \tag{8}$$

where τ_0 is the optical depth at the line center, and $\phi(\lambda)$ is the line profile, which is assumed to have Gaussian shape. The line center optical depth is calculated by

$$\tau_0 = \frac{\sqrt{\pi} e^2 \lambda_{\rm c} f_\lambda}{m_{\rm e} c} \left(\frac{M_{\rm i}}{2T_{\rm i}}\right)^{1/2} N_{\rm l}, \tag{9}$$

where $\lambda_{\rm c}$ is the line center wavelength, f_λ is the oscillator strength, $m_{\rm e}$ is the electron mass, $N_{\rm l} = \int n_{\rm l}\, {\rm dl}$ is the column density of the lower level from the point of emission to the spectrometer, $M_{\rm i}$ is the ion mass and ion temperature $T_{\rm i} = T_{\rm e}$[33].

As the Einstein A coefficient is proportional to f_λ, lines which have strong transition probability have a greater probability of being absorbed as well. This is especially true for the He-α resonance line, while the intercombination and forbidden lines' absorption is much lower, owing to the lower A coefficient. In fact, the difference of six orders of magnitude between the A coefficients of the resonance line ($A = 3.76 \times 10^{13}\,{\rm s}^{-1}$) and the intercombination line ($A = 1.04 \times 10^{7}\,{\rm s}^{-1}$) indicates that the resonance line has reached its BB limit [23], while the intercombination line goes through a transparent medium. This explains the greatly reduced value of the resonance line relative to the other He-α ones. Regarding the satellite lines, some of these have large A coefficients. For instance, the A coefficient of the 1s2p^2 ^{2}P$_{1/2}$ → 1s^{2}2p ^{2}P$_{1/2}$ transition is $A = 3.31 \times 10^{13}\,{\rm s}^{-1}$. Several other transitions, also have A coefficients of the order of $10^{13}\,{\rm s}^{-1}$. These lines are also greatly reduced for the same reason as for the resonance line.

Model 3 uses the same input parameters as Model 1. The red line in Figure 6 is the simulation result of Model 3. Compared with the optically thin model, the resonance line and the satellite line of the Li-like ion are reduced by PR so much that they are comparable to the intercombination line. It turns out that the result of Model 3 is much closer to the experimental spectrum than the previous results.

In Model 3, the column density of the He-like ion is $N_{\rm Si^{12+}} = 0.74 \times 10^{17}$ cm^{-2}, but $N_{\rm Si^{12+}}$ is always smaller than 0.6×10^{17} cm^{-2} in Model 2. Even if PR was added into the time-dependent model, it would not have sufficient absorption. For a bigger value of $N_{\rm Si^{12+}}$ in the time-dependent model, it again needs a larger dilution factor, which was not tried in this study. Considering the present result is much closer than the previous results and the time-dependent model consumes much more CPU time than the steady-state model, we think that a steady-state optically thick model is sufficient to simulate the Fujioka *et al*. photoionization experiment.

https://doi.org/10.1017/hpl.2020.49 Published online by Cambridge University Press

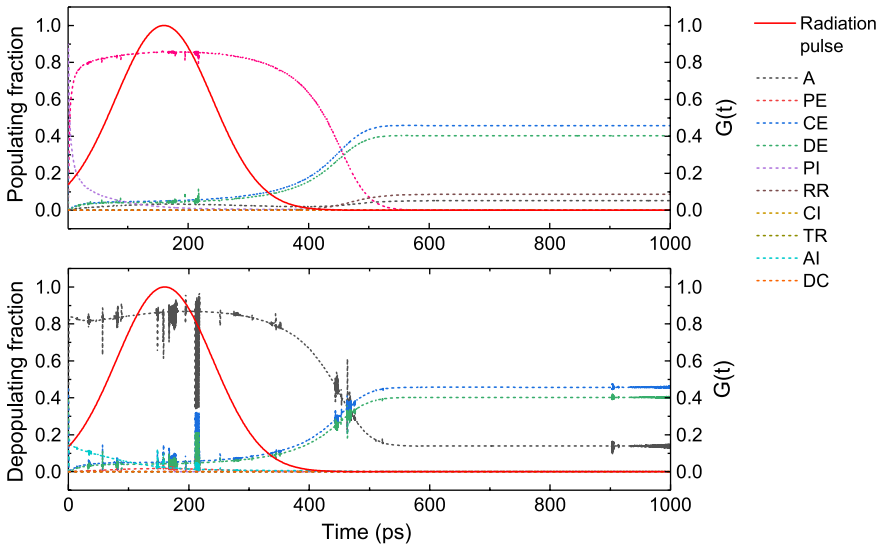

Figure 5. Evolution of process contributions to 1s2p $^1P_1$. Upper panel: populating contributions. Lower panel: depopulating contributions. The radiation pulse is also plotted.

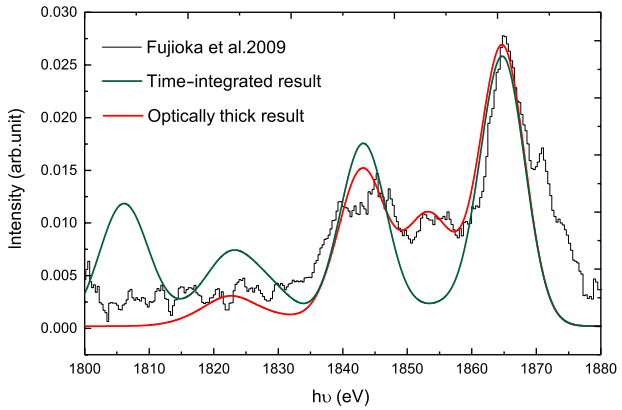

Figure 6. Black line: the experimental spectrum of Fujioka *et al.*[13]. Green line: theoretical spectrum of time-dependent model. Red line: theoretical spectrum of optically thick model.

3.4. Line ratios

Now that the experimental spectrum is successfully explained by an optically thick model, the line ratios of He-α triplet lines need to be rediscussed. There are two important line ratios for the He-α triplet,

$$G = \frac{I_F + I_I}{I_R}, \tag{10}$$

and

$$R = \frac{I_F}{I_I}, \tag{11}$$

where I_R, I_I and I_F are the intensities of the resonance, intercombination and forbidden lines, respectively. Gabriel and Jordan proposed that G is sensitive to the electron temperature and R is relative to the electron density, and these two ratios have been widely applied to diagnose the electron temperature and electron density of photoionizing plasmas[34–37]. According to the above results, the line ratios are influenced by the satellite lines and the PR effect. The He-α lines are surrounded by a lot of intense satellite lines, especially the forbidden line[19,25,38], and these can hardly be distinguished from each other. Thus, under some low resolution conditions, the influence of satellite lines needs to be taken into account in the calculation of line intensities. We denote by I_{R+}, I_{I+} and I_{F+} the intensities of the spectrum near three He-α lines, and the corresponding line ratios by R_+ and G_+[22,25]. Specified to the Fujioka *et al.* photoionization experiment, the forbidden line is invisible among the surrounding satellite lines, and it is impossible to get an exact I_F. It is easy to take the left peak as a unity and use the new line ratios to diagnose the electron density and temperature. Consequently, the experimental line ratios are $G_{e+} \sim 0.94$ and $R_{e+} \sim 2.09$. The optically thin model gives the traditional line ratios of $G_1 = 3.16 \times 10^{-2}$ and $R_1 = 1.61 \times 10^{-6}$, which have similar values of A coefficient and are hardly measurable in the experimental environment. The deduced ratios in Model 1 are $R_{1+} = 5.55$ and $G_{1+} = 0.39$, and in Model 3 are $R_{3+} = 1.02$ and $G_{3+} = 1.48$.

4. Conclusion

In this paper, the X-ray spectrum of photoionized silicon plasmas under the conditions of the Fujioka *et al.* photoionization experiment was investigated with a steady-state optically thin model, a time-dependent optically thin model and a steady-state optically thick model, respectively.

https://doi.org/10.1017/hpl.2020.49 Published online by Cambridge University Press

The following was found.

Photoexcitation produces a strong resonance line and some nearby Li-like lines because of large photoexcitation rates and lower-level densities. Consequently, these lines are much stronger than the forbidden line and intercombination line in the optically thin models (Model 1 and Model 2).

The resonance line and some satellite lines are easily absorbed as the photons travel to the detector. As a result, the experimental spectrum is successfully simulated by an optically thick model, where the intercombination lines become more visible than in previous studies.

The G and R ratios of He-α lines are influenced by the satellite lines, optical effect and plasma ionization structure. Therefore, one needs to be careful when using these line ratios in plasma diagnosis.

Acknowledgments

This work was supported by the Science Challenge Project (No. TZ2016005), the National Natural Science Foundation of China (Nos. 11903006, 12073043 and U1930108), and the Strategic Priority Research Program of Chinese Academy of Sciences (No. XDA25030700).

References

1. D. A. Liedahl, in *X-Ray Spectroscopy in Astrophysics* (Springer, Berlin, 1999), p. 189.
2. D. E. Osterbrock, *Astrophysics of Gaseous Nebulae and Active Galactic Nuclei* (University Science Books, Mill Valley, CA, 1989).
3. B. A. Remington, R. P. Drake, and D. D. Ryutov, Rev. Mod. Phys. **78**, 755 (2006).
4. H. Takabe, Prog. Theor. Phys. Supp. **143**, 202 (2001).
5. E. Behar and H. Netzer, Astrophys. J. **570**, 165 (2002).
6. C. B. Tarter, W. H. Tucker, and E. E. Salpeter, Astrophys. J. **156**, 943 (1969).
7. N. S. Schulz, C. R. Canizares, J. C. Lee, and M. Sako, Astrophys. J. Lett. **564**, L21 (2002).
8. S. Wat, M. Sako, M. Ishida, Y. Ishisaki, S. M. Kahn, T. Kohmura, F. Nagase, F. Paerels, and T. Takahashi, Astrophys. J. **651**, 421 (2006).
9. M. H. van Kerkwijk, J. van Paradijs, E. J. Zuiderwijk, G. Hammerschlag-Hensberge, L. Kaper, and C. Sterken, Astron. Astrophys. **303**, 483 (1995).
10. M. Sako, D. A. Liedahl, S. M. Kahn, and F. Paerels, Astrophys. J. **525**, 921 (1999).
11. F. Wang, D. Salzmann, G. Zhao, and H. Takabe, Astron. J. **144**, 122 (2012).
12. M. E. Foord, R. F. Heeter, P. A. van Hoof, R. S. Thoe, J. E. Bailey, M. E. Cuneo, H.-K. Chung, D. A. Liedahl, K. B. Fournier, G. A. Chandler, V. Jonauskas, R. Kisielius, L. P. Mix, C. Ramsbottom, P. T. Springer, F. P. Keenan, S. J. Rose, and W. H. Goldstein, Phys. Rev. Lett. **93**, 055002 (2004).
13. S. Fujioka, H. Takabe, N. Yamamoto, D. Salzmann, F. Wang, H. Nishimura, Y. Li, Q. Dong, S. Wang, Y. Zhang, Y. -J. Rhee, Y. -W. Lee, J. -M. Han, M. Tanabe, T. Fujiwara, Y. Nakabayashi, G. Zhao, J. Zhang, and K. Mima, Nat. Phys. **5**, 821 (2009).
14. S. Fujioka, N. Yamamoto, D. Salzmann, F. Wang, Y. Li, Q. Dong, S. Wang, Y. Zhang, Y.-J. Rhee, Y.-W. Lee, J.-M. Han, D.-H. Kwon, J. Zhong, G. Zhao, M. Tanabe, T. Fujiwara, Y. Nakabayashi, J. Zhang, H. Nishimura, H. Takabe, and K. Mima, Plasma Phys. Control. Fusion **51**, 124032 (2009).
15. D. Porquet, J. Dubau, and N. Grosso, Space Sci. Rev. **157**, 103 (2010).
16. F. L. Wang, D. Salzmann, G. Zhao, H. Takabe, S. Fujioka, N. Yamamoto, H. Nishimura, and J. Zhang, Astrophys. J. **706**, 592 (2009).
17. L. Bao, Z. Wu, B. Duan, Y. Ding, and J. Yan, Phys. Plasmas **18**, 023301 (2011).
18. E. Hill and S. Rose, Phys. Plasmas **17**, 103301 (2010).
19. B. Han, F. Wang, G. Liang, and G. Zhao, Acta Phys. Sin. **65**, 110503 (2016).
20. Z. Wu, B. Duan, Y. Li, and J. Yan, High Energy Density Phys. **23**, 153 (2017).
21. B. Han, F. Wang, D. Salzmann, and G. Zhao, Publ. Astron. Soc. Jpn. **67**, 29 (2015).
22. B. Han, F. Wang, J. Zhong, G. Liang, H. Wei, D. Yuan, B. Zhu, F. Li, C. Liu, Y. Li, J. Zhao, Z. Zhang, C. Wang, J. Xiong, G. Jia, N. Hua, J. Zhu, Y. Li, G. Zhao, and J. Zhang, High Power Laser Sci. Eng. **6**, e31 (2018).
23. D. Salzmann, *Atomic Physics in Hot Plasmas* (Oxford University Press, New York, 1998).
24. M. F. Gu, Can. J. Phys. **86**, 675 (2008).
25. F. Wang, B. Han, D. Salzmann, and G. Zhao, Phys. Plasmas **24**, 041403 (2017).
26. N. R. Badnell, J. Phys. B **18**, 955 (1985).
27. J. Davis, P. C. Kepple, and M. Blaha, J. Quant. Spectrosc. Radiat. Transf. **18**, 535 (1977).
28. M. Jones, Mon. Not. R. Astron. Soc. **169**, 211 (1974).
29. D. H. Sampson and R. E. H. Clark, Astrophys. J. Supp. Ser. **44**, 169 (1980).
30. J. C. Stewart and K. D. Pyatt Jr., Astrophys. J. Lett. **144**, 1203 (1966).
31. T. Kallman and M. Bautista, Astrophys. J. Supp. Ser. **133**, 221 (2001).
32. M. Mehdipour, J. S. Kaastra, and A. J. J. Raassen, Astron. Astrophys. **579**, A87 (2015).
33. A. K. Pradhan and S. N. Nahar, *Atomic Astrophysics and Spectroscopy* (Cambridge University Press, New York, 2015).
34. D. Porquet and J. Dubau, Astron. Astrophys. Supp. Ser. **143**, 495 (2000).
35. A. H. Gabriel and C. Jordan, Nature **221**, 947 (1969).
36. A. H. Gabriel and C. Jordan, Mon. Not. R. Astron. Soc. **145**, 241 (1969).
37. L. Ji, N. Schulz, M. Nowak, H. L. Marshall, and T. Kallman, Astrophys. J. **700**, 977 (2009).
38. F. Wang, B. Han, R. Jin, D. Salzmann, G. Liang, H. Wei, J. Zhong, G. Zhao, and J. Li, J. Phys. B **49**, 064013 (2016).

https://doi.org/10.1017/hpl.2020.49 Published online by Cambridge University Press